Compliant Motion Control for Multisegment Continuum Robots With Actuation Force Sensing

Roger E. Goldman, *Member, IEEE*, Andrea Bajo, *Member, IEEE*, and Nabil Simaan, *Senior Member, IEEE*

***Abstract*—During exploration through tortuous unstructured passages by continuum robots, methods are required to minimize the force interaction between the environment and the robot along its length. This paper presents and evaluates an algorithm for compliant motion control of continuum robots subjected to multiple unknown contacts with the environment. A mapping of external wrenches to a generalized force in the configuration space of a multisegment continuum robot is presented and related to measured joint-level actuation forces. These measurements are applied as inputs to a low-level compliant motion controller. Friction and modeling uncertainties, presenting an unknown nonlinear deviation from the nominal system model, are corrected via a feed-forward estimate provided by a support vector machine. The controller is evaluated on Ø9 and Ø5 mm multisegment continuum robots. We quantify the minimal interaction forces needed to generate compliant motion and demonstrate the ability of the controller to minimize interaction forces during insertion through tortuous passages.**

***Index Terms*—Compliant motion control, continuum robot, machine learning, support vector machine.**

I. Introduction

CONTINUUM robots differ from traditional articulated robots in that motion is generated by structural deformation as opposed to the relative motion of individual rigid links. Hirose [1], Robinson and Davies [2], and Webster and Jones [3] offer surveys of the design types and general applications for continuum robots. Investigators have proposed continuum robot structures for disaster relief [4], [5], nuclear handling [6], and minimally invasive surgery [7]–[10].

A limitation to adoption of continuum robots in these applications is the lack of control methods to prevent damage to the robot and the environment. During insertion into an unknown environment, these robots must interact safely while subjected to a multitude of unknown contacts along their length. There is a need for control algorithms that support safe interaction during the insertion process to avoid damage to both the robot and the environment. Ideally, these algorithms should not rely on expensive and complex technologies for sensing contact locations [11]. In this paper, we address these challenges by providing a methodology for compliant motion control for continuum robots without explicit knowledge of the environment or direct measurement of the interaction.

Of particular relevance to the task of compliant insertion are works demonstrating *whole arm* manipulation where the robot interacts with the environment along its entire length. Salisbury *et al.* [12] presented a mechanical and controller design for a whole-arm manipulator. Mochiyama *et al.* [13] proposed a method for grasping using a shape descriptor for multiple contacts of a high degrees of freedom (DoF) robot. Park and Khatib [14] investigated algorithms for force control at known multiple contact points with redundant manipulators. While generally applicable to rigid robots, these works cannot be directly applied to continuum robots.

Passive compliance has been proposed to achieve safe interaction without the need for additional sensing and complex control. Cable-driven [9], [10], [15], [16], shape memory alloy actuated [17]–[20], and pneumatic-driven structures [21], [22] have been used to provide passive compliance. Although these systems have shown promise in providing a measure of safety, they suffer from a number of disadvantages for exploration and manipulation in unstructured environments. They are limited in the magnitude of forces that can be applied during environment interaction, and the measure of safety provided by the passive compliance is limited by the passive flexibility. Additionally, the compliance degrades trajectory tracking performance. Thus, a need exists for active compliant robots that can safely interact with the surrounding environment while maintaining manipulation precision and delivering adequate force for executing manipulation tasks.

Active compliance has been evaluated under limited conditions for continuum robots. Mahvash and Dupont [23] presented an active stiffness controller that may be approximated by a Cosserat rod subjected to a wrench at the end effector. Giri and Walker [24] investigate underactuated grasping with continuum robots based on a kinematic model. To date, no investigation has addressed the need for compliant control of continuum robots subjected to multiple whole-arm contacts.

The environment interaction forces at the tip of a continuum robot actuated by backbones may be estimated using backbone actuation force measurements. This was demonstrated by Xu and Simaan [25], [26] for force sensing at the operational point and by Bajo and Simaan [27] for contact detection. Our approach

Manuscript received May 30, 2013; revised November 1, 2013; accepted February 28, 2014. Date of publication March 26, 2014; date of current version August 4, 2014. This paper was recommended for publication by Associate Editor Y. Choi and Editor B. J. Nelson upon evaluation of the reviewers' comments. The work of N. Simaan and A. Bajo was supported in part by the National Science Foundation under Career Grant IIS-1063750.

R. E. Goldman is with the Department of Internal Medicine, Crozer Chester Medical Center, Upland, PA 19013 USA (e-mail: rogergoldman@gmail.com).

A. Bajo is with MAKO Surgical Corp., Fort Lauderdale, FL 33317 USA (e-mail: andrea.bajo@gmail.com).

N. Simaan is with the Department of Mechanical Engineering, Vanderbilt University, Nashville, TN 37240 USA (e-mail: nabil.simaan@vanderbilt.edu).

Color versions of one or more of the figures in this paper are available online at http://ieeexplore.ieee.org.

Digital Object Identifier 10.1109/TRO.2014.2309835

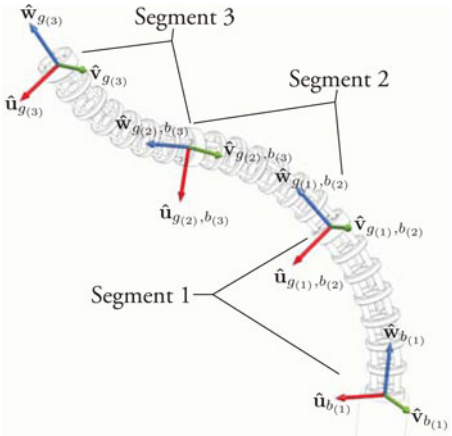

Fig. 1. Model with coordinate systems for a three segment continuum robot.

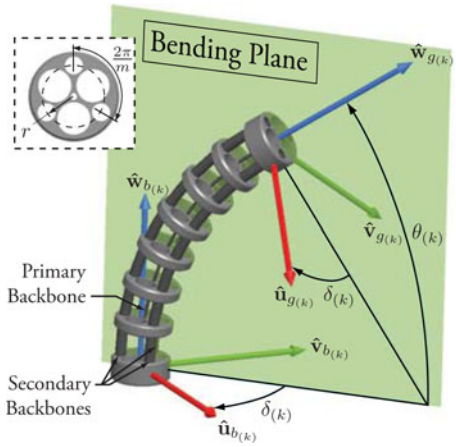

Fig. 2. Structure and kinematic nomenclature for the kth segment of a multisegment continuum robot.

leverages the remote sensing capabilities of continuum robots to provide compliant motion control without explicit information of the wrench[1] location and magnitude.

The contributions of this paper are in presenting new frameworks for controlling continuum robots subject to whole-arm contacts. In [28], we proposed a compliant motion control for a single-segment robot performing planar bending. This paper generalizes our approach to enable compliant motion control for multisegment continuum robots operating in multiple DoF. In addition, this study more thoroughly quantifies the performance of the controller. A novel mapping of the environment wrenches to a *generalized force* in the configuration space of a continuum segment is defined. A closed-form analytic expression of the stiffness of a continuum robot driven by nickel titanium (NiTi) tubes and wires is defined based on an expression of the system energy. A compliant motion controller is proposed to drive a continuum robot segment to a configuration that minimizes its interaction with *unknown* wrenches acting at *unknown* locations. The controller uses the difference between the measured and predicted unperturbed generalized force to move in a direction to minimize the environment interaction. Estimation of model uncertainties by a support vector regression (SVR) obviates the need for an exact model of friction parameters and provides robustness to model uncertainties. This study supports safe deployment of continuum structures into unstructured environments with intelligent control for minimization of environment interaction.

II. Model Description

A. Continuum Robot System

The continuum robots analyzed and demonstrated in this paper are multibackbone multisegment robots constructed with NiTi backbones. Fig. 1 depicts a model of a three segment continuum robot. Each segment is composed of several secondary backbones, a single central backbone, an end disk, a base disk, and spacer disks. The secondary backbones are superelastic NiTi tubes circumferentially distributed around a central backbone along a pitch circle of radius r. The end disk is attached to all backbones, while the base disk is only attached to the central backbone. The spacer disks are separated by elastomeric spacers and float along the central backbone while maintaining a fixed radial distance between the central backbone and all secondary backbones. Using this arrangement, two DoF per segment are controlled by pushing and pulling on the secondary backbones to bend the segment.

The individual segments of the continuum robot are serially stacked yielding $2n$ DoF for n segments. The secondary backbones of distal segments run concentrically through those of proximal segments creating a compact structure.

[1]A wrench is defined as a 6-D vector composed of a force vector followed by a moment vector.

B. Nomenclature

The following nomenclature described below and shown in Figs. 1 and 2 is used to facilitate mathematical modeling.

$\mathbf{A}_i$	ith row of $\mathbf{A}$.
$\mathbf{A}^{[i]}$	ith column of $\mathbf{A}$.
$[\mathbf{A}]_{ij}$	Entry at the ith row and jth column of the matrix $\mathbf{A}$.
n	Number of segments of the continuum robot.
m	Number of secondary backbones in each continuum segment.
c_α, s_α	Abbreviated form of the cosine and sine, respectively, where $\mathrm{c}_\alpha \triangleq \cos(\alpha)$ and $\mathrm{s}_\alpha \triangleq \sin(\alpha)$.
$\theta_{(k)}$	Bending angle for the k'th segment.
$\delta_{(k)}$	Bending plane angle of the k'th segment.
$\boldsymbol{\psi}_{(k)}$	Configuration space vector for the k'th segment, $\boldsymbol{\psi}_{(k)} = [\theta_{(k)}, \delta_{(k)}]^{\mathrm{T}}$.
$\boldsymbol{\psi}_a$	Augmented configuration space vector for the multisegment continuum robot $\boldsymbol{\psi}_a = [\boldsymbol{\psi}_{(1)}^{\mathrm{T}}, \ldots, \boldsymbol{\psi}_{(n)}^{\mathrm{T}}]^{\mathrm{T}}$.
$\hat{\mathbf{u}}$, $\hat{\mathbf{v}}$, $\hat{\mathbf{w}}$	Unit basis vectors of an arbitrary coordinate frame such that $[\,\hat{\mathbf{u}}, \quad \hat{\mathbf{v}}, \quad \hat{\mathbf{w}}\,] = \mathbf{I} \in \mathbb{R}^{3\times 3}$.
$\{b_{(k)}\}$	Base frame of the kth segment.
$\{g_{(k)}\}$	End frame of the kth segment.
${}^c\mathbf{p}_{ab}$	Position vector pointing from point $\mathbf{a}$ (or the origin of frame $\{a\}$) to point $\mathbf{b}$ (or the origin of frame $\{b\}$) expressed in frame $\{c\}$.

${}^{a}\mathbf{R}_{b}$	Rotation matrix describing the orientation of frame $\{b\}$ with respect to frame $\{a\}$.
${}^{c}\mathbf{v}_{b/a}$	Linear velocity of frame $\{b\}$ with respect to frame $\{a\}$, expressed in frame $\{c\}$.
${}^{c}\boldsymbol{\omega}_{b/a}$	Angular velocity of frame $\{b\}$ with respect to frame $\{a\}$, expressed in frame $\{c\}$.
${}^{c}\mathbf{t}_{b/a}$	Twist of frame $\{b\}$ with respect to frame $\{a\}$, expressed in frame $\{c\}$: ${}^{c}\mathbf{t}_{b/a} = \left[{}^{c}\mathbf{v}_{b/a}^{\mathrm{T}}, \quad {}^{c}\boldsymbol{\omega}_{b/a}^{\mathrm{T}}\right]^{\mathrm{T}}$.
$\mathbf{J}_{\mathbf{q}\boldsymbol{\psi}_{(k)}}$	A Jacobian matrix linearly mapping the configuration space velocities to joint velocities such that $\dot{\mathbf{q}}_{(k)} = \mathbf{J}_{\mathbf{q}\boldsymbol{\psi}_{(k)}}\dot{\boldsymbol{\psi}}_{(k)}$.
$\mathbf{J}_{\mathbf{v}\boldsymbol{\psi}_{(k)}}$	A Jacobian matrix linearly mapping the configuration space velocities to linear velocities such that $\dot{\mathbf{v}} = \mathbf{J}_{\mathbf{v}\boldsymbol{\psi}_{(k)}}\dot{\boldsymbol{\psi}}_{(k)}$.
$\mathbf{J}_{\boldsymbol{\omega}\boldsymbol{\psi}_{(k)}}$	A matrix linearly mapping of the configuration space velocities to angular velocities such that $\dot{\boldsymbol{\omega}} = \mathbf{J}_{\boldsymbol{\omega}\boldsymbol{\psi}_{(k)}}\dot{\boldsymbol{\psi}}_{(k)}$.
$\mathbf{J}_{\mathbf{t}\boldsymbol{\psi}_{(k)}}$	A linear mapping of the configuration space velocities to the twist such that $\mathbf{t} = \mathbf{J}_{\mathbf{t}\boldsymbol{\psi}_{(k)}}\dot{\boldsymbol{\psi}}_{(k)}$ and $\mathbf{J}_{\mathbf{t}\boldsymbol{\psi}_{(k)}} = \begin{bmatrix} \mathbf{J}_{\mathbf{v}\boldsymbol{\psi}_{(k)}} \\ \mathbf{J}_{\boldsymbol{\omega}\boldsymbol{\psi}_{(k)}} \end{bmatrix}$.
E_Y	Young's elasticity modulus for the NiTi backbones.
$I_{(k)}$	Cross-sectional second moment of inertia of backbones of the kth segment.
r	Radius of the pitch circle along which the secondary backbones are circumferentially distributed.
$L_{j,(k)}$	Length of the jth secondary backbone of the kth segment for $j = 1, \ldots, m$.
$L_{(k)}$	Length of the primary backbone of the kth segment.
$\boldsymbol{\tau}_{(k)}$	Backbone actuation forces of an individual segment $\boldsymbol{\tau}_{(k)} = \left[\tau_{1,(k)}, \ \ldots, \ \tau_{m,(k)}\right]^{\mathrm{T}}$.
$\mathbf{f}_{(k)}$	Generalized force for the kth segment.
$\mathbf{f}_a$	Augmented generalized force for the multi-segment continuum robot $\mathbf{f}_a = \left[\mathbf{f}_{(1)}^T, \ \ldots, \ \mathbf{f}_{(n)}^T\right]^T$.
$\mathbf{w}_{e,(k)}$	External wrench applied to the end disk of the kth segment.
$\boldsymbol{\lambda}, \hat{\boldsymbol{\lambda}}$	Actual and estimated augmented generalized force errors.
$\mathbf{K}_{\boldsymbol{\psi},(k)}$	Configuration space stiffness for the kth segment.
$\mathbf{K}_{\boldsymbol{\psi}_a}$	Configuration space stiffness for the multisegment continuum robot.
$\mathbf{x}$	Input feature vector to the SVR.
N	The number of training data for the SVR optimization.
$\boldsymbol{\varphi}(\cdot)$	High-dimensional mapping of the input feature space of the support vectors in the SVR.
ϵ	Unpenalized (Vapnik's) error in SVR.
γ	Weighting parameter of the radial basis function.
$\boldsymbol{\alpha}$, $\boldsymbol{\alpha}^*$	Lagrange multipliers for SVR optimization.
$\mathbf{a}$	Weights for support vectors in SVR.

III. Segment Kinematics and Statics

The kinematics and statics are developed in this section for subsequent derivation of the stiffness and controller in Sections IV and V. The kinematics of continuum robots has been thoroughly investigated using an assumption that individual segments bend in circular arcs, e.g., [3], [7], [8], [29], [30]. We adopt this assumption as it has been validated by Xu and Simaan [26] for small continuum robots with appropriately distributed spacer disks. Deviations from this model will be addressed by uncertainty estimation in Section V-C.

The pose of the kth segment is described in a set of generalized coordinates by a *configuration space* vector as

$$\boldsymbol{\psi}_{(k)} = \left[\theta_{(k)}, \ \delta_{(k)}\right]^{\mathrm{T}} \tag{1}$$

where $(\cdot)_{(k)}$ denotes a variable associated with the kth segment. Referring to Fig. 2, $\theta_{(k)}$ is the segment bending angle measured between the plane of the base disk, $\{\hat{\mathbf{u}}_{b_{(k)}}, \hat{\mathbf{v}}_{b_{(k)}}\}$, and the direction the normal to the end disk $\hat{\mathbf{w}}_{g_{(k)}}$. The angle $\delta_{(k)}$ defines the orientation of the segment bending plane as measured from the plane to $\hat{\mathbf{u}}_{b_{(k)}}$ about $\hat{\mathbf{w}}_{b_{(k)}}$.

The inverse kinematics of the segment relating the configuration space, $\boldsymbol{\psi}_{(k)}$, to the joint space, $\mathbf{q}_{(k)} = \left[q_{1,(k)}, \ q_{2,(k)}, \ldots, \ q_{m,(k)}\right]^{\mathrm{T}}$, is given by

$$L_{j,(k)} = L_{(k)} + q_{j,(k)} = L_{(k)} + \Delta_{j,(k)}\Theta_{(k)} \tag{2}$$

where $\Delta_{j,(k)} = r\cos\sigma_{j,(k)}$, $\sigma_{j,(k)} = \delta_{(k)} + (j-1)\frac{2\pi}{m}$, and $\Theta_{(k)} = \theta_{(k)} - \frac{\pi}{2}$.

Differentiating (2) with respect to time yields the instantaneous inverse kinematics

$$\dot{\mathbf{q}}_{(k)} = \mathbf{J}_{\mathbf{q}\boldsymbol{\psi}_{(k)}}\dot{\boldsymbol{\psi}}_{(k)} \tag{3}$$

where the Jacobian $\mathbf{J}_{\mathbf{q}\boldsymbol{\psi}_{(k)}}$ is given by

$$\mathbf{J}_{\mathbf{q}\boldsymbol{\psi}_{(k)}} = \begin{bmatrix} r\mathrm{c}_{\sigma_{1,(k)}} & -r\Theta_{(k)}\mathrm{s}_{\sigma_{1,(k)}} \\ \vdots & \vdots \\ r\mathrm{c}_{\sigma_{m,(k)}} & -r\Theta_{(k)}\mathrm{s}_{\sigma_{m,(k)}} \end{bmatrix}. \tag{4}$$

The direct kinematics of the kth segment is given by the position ${}^{b_{(k)}}\mathbf{p}_{b_{(k)}g_{(k)}}$ and orientation ${}^{b_{(k)}}\mathbf{R}_{g_{(k)}}$. For $\theta_{(k)} \neq \frac{\pi}{2}$, the kinematics takes the form

$${}^{b_{(k)}}\mathbf{p}_{b_{(k)}g_{(k)}} = \frac{L_{(k)}}{\Theta_{(k)}}\begin{bmatrix} \mathrm{c}_{\delta_{(k)}}\left(\mathrm{s}_{\theta_{(k)}} - 1\right) \\ -\mathrm{s}_{\delta_{(k)}}\left(\mathrm{s}_{\theta_{(k)}} - 1\right) \\ -\mathrm{c}_{\theta_{(k)}} \end{bmatrix} \tag{5}$$

$${}^{b_{(k)}}\mathbf{R}_{g_{(k)}} = e^{-\delta_{(k)}[\hat{\mathbf{w}}\times]}e^{-\Theta_{(k)}[\hat{\mathbf{v}}\times]}e^{\delta_{(k)}[\hat{\mathbf{w}}\times]} \tag{6}$$

where $\hat{\mathbf{v}} = [0, \ 1, \ 0]^{\mathrm{T}}$, $\hat{\mathbf{w}} = [0, \ 0, \ 1]^{\mathrm{T}}$, and the frames $\{g_{(k)}\}$ and $\{b_{(k)}\}$ are shown in Fig. 2. For $\theta_{(k)} = \frac{\pi}{2}$, the formulation singularity, $\frac{1}{\Theta_{(k)}}$, resolves to

$${}^{b_{(k)}}\mathbf{p}_{b_{(k)}g_{(k)}} = \begin{bmatrix} 0 & 0 & L_{(k)} \end{bmatrix}^{\mathrm{T}} \tag{7}$$

$${}^{b_{(k)}}\mathbf{R}_{g_{(k)}} = \mathbf{I} \in \mathbb{R}^{3\times 3}. \tag{8}$$

By differentiating (5) and (6), the instantaneous direct kinematics takes the form

$${}^{b_{(k)}}\mathbf{t}_{g_{(k)}/b_{(k)}} = \mathbf{J}_{\mathbf{t}\boldsymbol{\psi}_{(k)}}\dot{\boldsymbol{\psi}}_{(k)} \tag{9}$$

where, for $\theta_{(k)} \neq \frac{\pi}{2}$, the Jacobian $\mathbf{J}_{\mathbf{t}\boldsymbol{\psi}_{(k)}}$ is given by

$$\mathbf{J}_{\mathbf{t}\boldsymbol{\psi}_{(k)}} = \begin{bmatrix} L_{(k)}\mathrm{c}_{\delta_{(k)}} \dfrac{\Theta_{(k)}\mathrm{c}_{\theta_{(k)}} - \mathrm{s}_{\theta_{(k)}} + 1}{\Theta_{(k)}^2} & -L_{(k)}\mathrm{s}_{\delta_{(k)}} \dfrac{\mathrm{s}_{\theta_{(k)}} - 1}{\Theta_{(k)}} \\ -L_{(k)}\mathrm{s}_{\delta_{(k)}} \dfrac{\Theta_{(k)}\mathrm{c}_{\theta_{(k)}} - \mathrm{s}_{\theta_{(k)}} + 1}{\Theta_{(k)}^2} & -L_{(k)}\mathrm{c}_{\delta_{(k)}} \dfrac{\mathrm{s}_{\theta_{(k)}} - 1}{\Theta_{(k)}} \\ L_{(k)} \dfrac{\Theta\mathrm{s}_{\theta_{(k)}} + \mathrm{c}_{\theta_{(k)}}}{\Theta_{(k)}^2} & 0 \\ -\mathrm{s}_{\delta_{(k)}} & \mathrm{c}_{\delta_{(k)}}\mathrm{c}_{\theta_{(k)}} \\ -\mathrm{c}_{\delta_{(k)}} & -\mathrm{s}_{\delta_{(k)}}\mathrm{c}_{\theta_{(k)}} \\ 0 & -1 + \mathrm{s}_{\theta_{(k)}} \end{bmatrix} \tag{10}$$

and, for $\theta_{(k)} = \frac{\pi}{2}$, the formulation singularity, $\frac{1}{\Theta_{(k)}}$, is resolved by applying l'Hôpital's rule [25], to yield

$$\mathbf{J}_{\mathbf{t}\boldsymbol{\psi}_{(k)}} = \begin{bmatrix} -\dfrac{L_{(k)}}{2}\mathrm{c}_{\delta_{(k)}} & \dfrac{L_{(k)}}{2}\mathrm{s}_{\delta_{(k)}} & 0 & -\mathrm{s}_{\delta_{(k)}} & -\mathrm{c}_{\delta_{(k)}} & 0 \\ 0 & 0 & 0 & 0 & 0 & 0 \end{bmatrix}^{\mathrm{T}}. \tag{11}$$

Using Euler beam bending analysis and neglecting gravitational potential energy as was justified by Xu and Simaan [25] for small continuum robots, the total energy of the continuum robot is given by $U = \sum_{k=1}^{n} U_{(k)}$, where the potential elastic energy of the kth segment is given by

$$U_{(k)} = \frac{E_Y I_{(k)} \Theta_{(k)}^2}{2} \left(\frac{1}{L_{(k)}} + \sum_{j=1}^{m} \frac{1}{L_{j,(k)}} \right). \tag{12}$$

Following the method of Simaan [7], the principle of virtual work and the energy expression (12) are used to obtain a statics model for the kth continuum segment as

$$\mathbf{J}_{\mathbf{q}\boldsymbol{\psi}_{(k)}}^{\mathrm{T}} \boldsymbol{\tau}_{(k)} = \nabla U_{(k)} - \mathbf{J}_{\mathbf{t}\boldsymbol{\psi}_{(k)}}^{\mathrm{T}} \mathbf{w}_{e,(k)} \tag{13}$$

where $\boldsymbol{\tau}_{(k)}$ represents the actuation forces on the secondary backbones, $\nabla U_{(k)}$ is the gradient of the potential energy, and $\mathbf{w}_{e,(k)}$ is the external wrench applied to the end disk of the kth continuum segment. The energy gradient $\nabla U_{(k)}$ is calculated with respect to a virtual displacement in configuration space, $\triangle\boldsymbol{\psi}_{(k)} = \left[\triangle\theta_{(k)},\ \triangle\delta_{(k)}\right]^{\mathrm{T}}$, and is given by

$$\nabla U_{(k)} = E_Y I_{(k)} \begin{bmatrix} \dfrac{\Theta_{(k)}}{L_{(k)}} + \displaystyle\sum_{j=1}^{m} \frac{\Theta_{(k)}}{L_{j,(k)}} - \frac{\Theta_{(k)}^2}{2} r \sum_{j=1}^{m} \frac{\mathrm{c}_{\sigma_{j,(k)}}}{L_{j,(k)}^2} \\ \dfrac{\Theta_{(k)}^3}{2} r \displaystyle\sum_{j=1}^{m} \frac{\mathrm{s}_{\sigma_{j,(k)}}}{L_{j,(k)}^2} \end{bmatrix}. \tag{14}$$

IV. Generalized Force and Stiffness

Equation (13) projects the actuation forces $\boldsymbol{\tau}_{(k)}$ and perturbation wrench $\mathbf{w}_{e,(k)}$ into the configuration space of the continuum segment $\boldsymbol{\psi}_{(k)}$. Thus, after projecting the 6-D wrench into the configuration space, the summation of the external interaction forces and torques on the segment resides in the vector space controllable within the framework of the single-segment kinematics, as specified by (1). We use this projection to eliminate the requirements for explicit determination of wrenches required by conventional compliance algorithms (e.g., [31]) and as a method for casting the interaction force minimization problem into the configuration space of the continuum segment.

Let the wrench acting on the end disk and projected into the configuration space be given as the generalized force vector

$$\mathbf{f}_{(k)} = \mathbf{J}_{\mathbf{t}\boldsymbol{\psi}_{(k)}}^{\mathrm{T}} \mathbf{w}_{e,(k)}. \tag{15}$$

For small perturbations from static equilibrium, the configuration space stiffness of the continuum segment is given by

$$\mathbf{K}_{\boldsymbol{\psi}} = \frac{d\mathbf{f}_{(k)}}{d\boldsymbol{\psi}_{(k)}} = \frac{\partial \mathbf{J}_{\mathbf{t}\boldsymbol{\psi}_{(k)}}^{\mathrm{T}}}{\partial \boldsymbol{\psi}_{(k)}} \mathbf{w}_{e,(k)} + \mathbf{J}_{\mathbf{t}\boldsymbol{\psi}_{(k)}}^{\mathrm{T}} \frac{\partial \mathbf{w}_{e,(k)}}{\partial \boldsymbol{\psi}_{(k)}} \tag{16}$$

where $\frac{\partial \mathbf{J}_{\mathbf{t}\boldsymbol{\psi}_{(k)}}^{\mathrm{T}}}{\partial \boldsymbol{\psi}_{(k)}}$ is a third-order tensor, and the product $\mathbf{J}_{\mathbf{t}\boldsymbol{\psi}_{(k)}}^{\mathrm{T}} \frac{\partial \mathbf{w}_{e,(k)}}{\partial \boldsymbol{\psi}_{(k)}}$ is calculated as defined in [32] and [33].

In the following, we make an assumption that the compliance motion control law is able to move the robot to maintain the external wrench $\mathbf{w}_{e,(k)}$ to be very small such that the term $\frac{\partial \mathbf{J}_{\mathbf{t}\boldsymbol{\psi}_{(k)}}^{\mathrm{T}}}{\partial \boldsymbol{\psi}_{(k)}} \mathbf{w}_{e,(k)}$ can be omitted in the subsequent derivations. We hence develop the configuration space stiffness model for an unloaded condition. This simplification is acceptable since the compliant motion controller designed in Section V requires an approximation of the robot stiffness to command a complaint motion that minimizes $\mathbf{w}_{e,(k)}$.

Applying (13) to the generalized force expression, the ith row of the generalized force $\mathbf{f}_{(k)}$ can be written as[2]

$$\mathbf{f}_i = \nabla U_i - \left[\mathbf{J}_{\mathbf{q}\boldsymbol{\psi}}^{\mathrm{T}}\right]_i \boldsymbol{\tau} = \nabla U_i - \left[\mathbf{J}_{\mathbf{q}\boldsymbol{\psi}}^{[i]}\right]^{\mathrm{T}} \boldsymbol{\tau} \tag{17}$$

where $\mathbf{J}_{\mathbf{q}\boldsymbol{\psi}}^{[i]}$ denotes the ith column of $\mathbf{J}_{\mathbf{q}\boldsymbol{\psi}}$.

Thus, the elements of $\mathbf{K}_{\boldsymbol{\psi}}$ are given by

$$\frac{\partial \mathbf{f}_i}{\partial \boldsymbol{\psi}_j} = \left[\mathbf{K}_{\boldsymbol{\psi}}\right]_{ij} = \frac{\partial}{\partial \boldsymbol{\psi}_j} \left[\nabla U_i - \left[\mathbf{J}_{\mathbf{q}\boldsymbol{\psi}}^{[i]}\right]^{\mathrm{T}} \boldsymbol{\tau} \right]. \tag{18}$$

The elements of $\mathbf{K}_{\boldsymbol{\psi}}$ can be expanded as

$$\left[\mathbf{K}_{\boldsymbol{\psi}}\right]_{ij} = \left[\mathbf{H}_{\boldsymbol{\psi}}\right]_{ij} - \left[\frac{\partial}{\partial \boldsymbol{\psi}_j} \left(\mathbf{J}_{\mathbf{q}\boldsymbol{\psi}}^{[\mathrm{i}]} \right) \right]^{\mathrm{T}} \boldsymbol{\tau} - \left[\mathbf{J}_{\mathbf{q}\boldsymbol{\psi}}^{[i]}\right]^{\mathrm{T}} \frac{\partial \boldsymbol{\tau}}{\partial \boldsymbol{\psi}_j} \tag{19}$$

where $\mathbf{H}_{\boldsymbol{\psi}}$ is the Hessian of the elastic energy of the segment. The elements of $\mathbf{H}_{\boldsymbol{\psi}}$ are given by

$$\frac{\partial^2 U}{\partial \theta^2} = E_Y I \left[\frac{1}{L} + \sum_{i=1}^{m} \frac{1}{L_i} - 2r\Theta \sum_{i=1}^{m} \frac{c_{\sigma_i}}{L_i^2} + \Theta^2 r^2 \sum_{i=1}^{m} \frac{c_{\sigma_i}^2}{L_i^3} \right] \tag{20}$$

$$\frac{\partial^2 U}{\partial \theta \partial \delta} = \frac{\partial^2 U}{\partial \delta \partial \theta} = E_Y I \left[\frac{3\Theta^2}{2} r \sum_{i=1}^{m} \frac{s_{\sigma_i}}{L_i^2} - \Theta^3 r^2 \sum_{i=1}^{m} \frac{s_{\sigma_i} c_{\sigma_i}}{L_i^3} \right] \tag{21}$$

$$\frac{\partial^2 U}{\partial \delta^2} = E_Y I \left[\frac{\Theta^3}{2} r \sum_{i=1}^{m} \frac{c_{\sigma_i}}{L_i^2} + \Theta^4 r^2 \sum_{i=1}^{m} \frac{s_{\sigma_i}^2}{L_i^3} \right]. \tag{22}$$

[2]The subscripted (k) denoting the kth segment will be dropped for (17) through (30) for ease of notation although it is understood that these equations are defined for the individual segment.

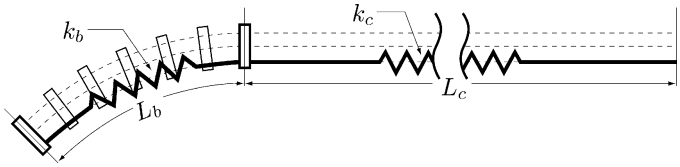

Fig. 3. Stiffness model for multibackbone continuum segment.

The second term of (19) expands to

$$\frac{\partial}{\partial \boldsymbol{\psi}_1}\left(\mathbf{J}^{[1]}_{\mathbf{q}\boldsymbol{\psi}}\right) = \mathbf{0} \in \mathbb{R}^m \tag{23}$$

$$\frac{\partial}{\partial \boldsymbol{\psi}_1}\left(\mathbf{J}^{[2]}_{\mathbf{q}\boldsymbol{\psi}}\right) = \frac{\partial}{\partial \boldsymbol{\psi}_2}\left(\mathbf{J}^{[1]}_{\mathbf{q}\boldsymbol{\psi}}\right) = -r\left[\mathrm{s}_{\sigma_1}, \ldots, \mathrm{s}_{\sigma_m}\right]^{\mathrm{T}} \tag{24}$$

$$\frac{\partial}{\partial \boldsymbol{\psi}_2}\left(\mathbf{J}^{[2]}_{\mathbf{q}\boldsymbol{\psi}}\right) = -r\Theta\left[\mathrm{c}_{\sigma_1}, \ldots, \mathrm{c}_{\sigma_m}\right]^{\mathrm{T}}. \tag{25}$$

Finally, the third term of (19) can be expanded by applying a simplifying assumption based on the relative geometry of the backbones in remote actuated continuum system configurations as explained below. The stiffness of the continuum robot, as measured from the actuation forces at the proximal end of the actuation lines, is a function of strain throughout the length of the actuation lines. Let the contributions to the axial stiffness be divided into the stiffnesses k_b and k_c, corresponding to the bending L_b and nonbending L_c regions of the actuation lines connecting the working distal end to the actuation unit (see Fig. 3).

The axial compliance along the length of a given actuation line can then be expressed as

$$\frac{1}{k} = \frac{1}{k_c} + \frac{1}{k_b} \tag{26}$$

where $k_c = \frac{E_Y A}{L_c}$ and $k_b = \frac{E_Y A}{L_b}$, and A denotes the cross-sectional area of the backbone.

For continuum robotic systems with remote actuation designed to access deep confined spaces, e.g., [8], [34], the lengths of the nonbending regions of the actuation lines far exceed that of the bending regions, $L_c \gg L_b$. The stiffness will, therefore, be dominated by the nonbending regions of the actuation lines. Local perturbations of the backbones at the actuation unit can be expressed as

$$\frac{\partial \boldsymbol{\tau}}{\partial \mathbf{q}} = \mathbf{K}_{\mathbf{q}} \tag{27}$$

where

$$\mathbf{K}_{\mathbf{q}} \cong \mathrm{diag}^3\left(\left[\frac{E_Y A}{L_c}, \ldots, \frac{E_Y A}{L_c}\right]\right) \in \mathbb{R}^{m\times m}. \tag{28}$$

Expanding terms by applying the chain rule and using the instantaneous inverse kinematics (3), $\dfrac{\partial \boldsymbol{\tau}}{\partial \boldsymbol{\psi}}$, is given by

$$\frac{\partial \boldsymbol{\tau}}{\partial \boldsymbol{\psi}} = \frac{\partial \boldsymbol{\tau}}{\partial \mathbf{q}}\frac{\partial \mathbf{q}}{\partial \boldsymbol{\psi}} \cong \mathbf{K}_{\mathbf{q}}\mathbf{J}_{\mathbf{q}\boldsymbol{\psi}}. \tag{29}$$

[3] $\mathrm{diag}(\mathbf{a})$ is the diagonalization of vector $\mathbf{a}$ or a block-diagonal matrix if array $\mathbf{a}$ contains matrices as its elements.

The configuration space stiffness, therefore, reduces to

$$[\mathbf{K}_{\boldsymbol{\psi}}]_{ij} = [\mathbf{H}_{\boldsymbol{\psi}}]_{ij} - \left[\frac{\partial}{\partial \boldsymbol{\psi}_j}\left(\mathbf{J}^{[\mathrm{i}]}_{\mathbf{q}\boldsymbol{\psi}}\right)\right]^{\mathrm{T}}\boldsymbol{\tau} - \left[\mathbf{J}^{[i]}_{\mathbf{q}\boldsymbol{\psi}}\right]^{\mathrm{T}}\mathbf{K}_{\mathbf{q}}\mathbf{J}^{[j]}_{\mathbf{q}\boldsymbol{\psi}}. \tag{30}$$

V. Compliant Motion Control

A. Controller Derivation

Using (15) and (30), a compliant motion controller can be constructed to minimize the difference between the expected and measured backbone actuation forces. Minimizing this difference minimizes the interaction force between the robot segment and the environment. The derivation seeks a form of $\dot{\boldsymbol{\psi}}_a$ based on the available measured data $\boldsymbol{\tau}_{(k)}$ and controlled parameters $\boldsymbol{\psi}_{(k)}$. This section begins by unifying the single-segment generalized force and stiffness into a multisegment framework. An error function for the controller is presented and related to the generalized force. Errors in the generalized force due to modeling uncertainties are discussed and a compensation term is formalized. Finally, the general multi-DoF multisegment compliant motion controller is proposed to minimize the error function.

The controller is formulated for compliant motion at each continuum segment subject to a perturbing wrench at the end disk of the segment. This wrench approximates a multitude of small perturbation forces acting along the length of a continuum segment during an insertion through a tortuous path. In an analogy to a linear spring model with an equilibrium position $f = k\,(x_{\mathrm{eq}} - x)$, there exists an equilibrium pose $\left\{{}^{b_{(k)}}\mathbf{p}_{\mathrm{eq}}, {}^{b_{(k)}}\mathbf{R}_{\mathrm{eq}}\right\}$, at which the wrench is minimized in the operation space of the continuum segment. Given this equilibrium position and the projection of the applied wrench to the configuration space, there exists a unique, although unknown, configuration $\boldsymbol{\psi}_{(k),d} = g\left({}^{b_{(k)}}\mathbf{p}_{\mathrm{eq}}, {}^{b_{(k)}}\mathbf{R}_{\mathrm{eq}}\right)$ that minimizes the wrench applied to the continuum segment. The objective of the compliance controller is to advance to this position using measurements of the backbone actuation forces $\boldsymbol{\tau}_{(k)}$ and therefore minimize the interaction wrench.

For multisegment continuum robots, a pose that minimizes the *augmented* generalized force on the system exists. Let

$$\mathbf{f}_a = \left[\mathbf{f}^{\mathrm{T}}_{(1)} \quad \cdots \quad \mathbf{f}^{\mathrm{T}}_{(n)}\right]^{\mathrm{T}} \tag{31}$$

be the augmented generalized force vector for an n-segment robot associated with the augmented configuration space

$$\boldsymbol{\psi}_a = \left[\boldsymbol{\psi}^{\mathrm{T}}_{(1)} \quad \cdots \quad \boldsymbol{\psi}^{\mathrm{T}}_{(n)}\right]^{\mathrm{T}}. \tag{32}$$

The configuration space stiffness of an individual segment is generalized to result in the augmented configuration space stiffness of the multisegment continuum robot as

$$\mathbf{K}_{\boldsymbol{\psi}_a} = \mathrm{diag}\left(\left[\mathbf{K}_{\boldsymbol{\psi},(1)}, \ldots, \mathbf{K}_{\boldsymbol{\psi},(n)}\right]\right). \tag{33}$$

We note that this model neglects kinematic and static coupling effects between subsequent segments. These coupling effects are minimized by the particular arrangement of the continuum robot where backbones of distal segments pass concentrically through the backbones of proximal segments as presented in Section II.

Let the error $\mathbf{e}_{\boldsymbol{\psi}_a}$ quantify the difference between the desired $\boldsymbol{\psi}_{a_d}$, and the current $\boldsymbol{\psi}_a$ configuration

$$\mathbf{e}_{\boldsymbol{\psi}_a} = \boldsymbol{\psi}_{a_d} - \boldsymbol{\psi}_a. \tag{34}$$

For a passive wrench condition, the equilibrium pose and corresponding configuration space remain fixed, e.g., $\dot{\boldsymbol{\psi}}_{a_d} = 0$. For external wrenches changing slowly with respect to the compliant control update rate, this condition becomes $\dot{\boldsymbol{\psi}}_{a_d} \approx 0$ and hence negligible when taking the time derivative of $\mathbf{e}_{\boldsymbol{\psi}_a}$. The following discussion uses $\dot{\boldsymbol{\psi}}_{a_d} = 0$ although it is to be understood that the same derivation follows for $\dot{\boldsymbol{\psi}}_{a_d} \approx 0$ by changing the equality sign to an approximation sign. The time derivative of the error function under these conditions becomes

$$\dot{\mathbf{e}}_{\boldsymbol{\psi}_a} = -\dot{\boldsymbol{\psi}}_a. \tag{35}$$

By assuming small perturbations and applying $\mathbf{K}_{\boldsymbol{\psi}_a}$, the error in the system can be related to $\mathbf{f}_a$ as

$$\mathbf{f}_a = \mathbf{K}_{\boldsymbol{\psi}_a} \mathbf{e}_{\boldsymbol{\psi}_a} \tag{36}$$

where $\triangle \mathbf{f}_a \cong \mathbf{f}_a$ for the small perturbations. This assumption holds for robots calibrated such that $\mathbf{f}_a \approx \mathbf{0}$ for unloaded movements and will be verified in Section VI.

During compliant motion control, the estimated generalized force $\hat{\mathbf{f}}_a$ is calculated using the idealized statics model of $\mathbf{f}_a$ based on the estimate of the energy and measured actuation forced as in (17). This estimate is contaminated by an uncertainty error $\boldsymbol{\lambda}$, due to unmodeled friction and strain along the actuation lines, perturbations from circular-bending shape of individual segments, deviations in the cross section of the backbones during bending, and uncertainties in the elastic properties of the NiTi backbones. Thus, without compensation, the generalized force estimate takes the form

$$\hat{\mathbf{f}}_{a,\text{uncompensated}} = \mathbf{f}_a + \boldsymbol{\lambda} \tag{37}$$

where $\mathbf{f}_a$ is given by (17).

A method to identify the generalized force error $\boldsymbol{\lambda}$ is to use its definition in (37) for movements of the continuum robot through its workspace with no externally applied wrenches. During this unloaded movement, the wrench at the end disk is $\mathbf{w}_e = \mathbf{0}$ and (15) predicts $\mathbf{f}_a = \mathbf{0}$. In an ideal continuum robot lacking backlash, friction, and other unmodeled effects, the prediction of the generalized force based on the measured values of the actuation forces $\boldsymbol{\tau}_{(k)}$ in (17) for each segment would also return $\mathbf{f}_a = \mathbf{0}$. However, the actual kinetostatic effects cause $\mathbf{f}_a \neq \mathbf{0}$, and this deviation forms $\boldsymbol{\lambda}$ that we seek to estimate. In order to compensate for the errors due to the interaction between segments, nonlinear regression via support vector (SV) machines is applied and evaluated in Section V-C. Other approaches as in [8] and [9] can be found for particular designs.

As will be verified experimentally, these model errors are highly dependent on the pose of the robot and the path in the configuration space to this pose. To compensate for the error, a feed-forward term is added to (37) to reduce the effects of $\boldsymbol{\lambda}$ during compliant motion control such that the compensated generalized force estimate is given by

$$\hat{\mathbf{f}}_a = \mathbf{f}_a + \boldsymbol{\lambda} - \hat{\boldsymbol{\lambda}} \tag{38}$$

where $\hat{\boldsymbol{\lambda}}$ is an estimate of the error, which will be defined using an SV machine in Section V-C.

An augmented compliant motion controller, accounting for the estimates of the unmodeled error $\hat{\boldsymbol{\lambda}}$ takes the form

$$\dot{\boldsymbol{\psi}}_a = \mu \mathbf{A} \hat{\mathbf{f}}_a \tag{39}$$

where μ and $\mathbf{A}$ correspond, respectively, to positive-definite scalar and matrix gains to be chosen by the operator in order to maximize the error correction while maintaining stability.

B. Controller Stability

Applying this compliant motion controller results in an asymptotically stable system, as will be shown using Lyapunov's direct method, in nonsingular configurations for any generalized force error meeting the requirement

$$\|\mathbf{e}_{\boldsymbol{\psi}_a}\| > \|\mathbf{K}_{\boldsymbol{\psi}_a}^{-1}(\boldsymbol{\lambda} - \hat{\boldsymbol{\lambda}})\|. \tag{40}$$

The above inequality ensures the controller error signal exceeds the noise caused by deviations from the ideal model corrected by the feed-forward estimate.

To prove the above result, we derive a new expression for the dynamics of the error in configuration space by applying (39) to (35) and accounting for (36) and (38) to yield

$$\dot{\mathbf{e}}_{\boldsymbol{\psi}_a} = -\mu \mathbf{A} \left(\mathbf{K}_{\boldsymbol{\psi}_a} \mathbf{e}_{\boldsymbol{\psi}_a} + \boldsymbol{\lambda} - \hat{\boldsymbol{\lambda}} \right). \tag{41}$$

A Lyapunov function candidate of the error system for compliant control (41) can be defined as

$$V(\mathbf{e}_{\boldsymbol{\psi}_a}) = \frac{1}{2} \mathbf{e}_{\boldsymbol{\psi}_a}^{\mathrm{T}} \mathbf{P} \mathbf{e}_{\boldsymbol{\psi}_a} \tag{42}$$

where $\mathbf{P}$ is any symmetric positive-definite matrix. Differentiating (42) with respect to time and accounting for (41) yields

$$\dot{V}(\mathbf{e}_{\boldsymbol{\psi}_a}) = \mathbf{e}_{\boldsymbol{\psi}_a}^{\mathrm{T}} \mathbf{P} \dot{\mathbf{e}}_{\boldsymbol{\psi}_a} = -\mu \mathbf{e}_{\boldsymbol{\psi}_a}^{\mathrm{T}} \mathbf{P} \mathbf{A} \left(\mathbf{K}_{\boldsymbol{\psi}_a} \mathbf{e}_{\boldsymbol{\psi}_a} + \boldsymbol{\lambda} - \hat{\boldsymbol{\lambda}} \right). \tag{43}$$

Choosing the control and Lyapunov weighting matrices as $\mathbf{A} = \mathbf{K}_{\boldsymbol{\psi}_a}^{-1}$ and $\mathbf{P} = \mathbf{I}$, result in

$$\dot{V}(\mathbf{e}_{\boldsymbol{\psi}_a}) = -\mu \left(\mathbf{e}_{\boldsymbol{\psi}_a}^{\mathrm{T}} \mathbf{e}_{\boldsymbol{\psi}_a} + \mathbf{e}_{\boldsymbol{\psi}_a}^{\mathrm{T}} \mathbf{K}_{\boldsymbol{\psi}_a}^{-1} (\boldsymbol{\lambda} - \hat{\boldsymbol{\lambda}}) \right). \tag{44}$$

Noting that the expression $\mathbf{e}_{\boldsymbol{\psi}_a}^{\mathrm{T}} \mathbf{e}_{\boldsymbol{\psi}_a}$ is positive definite for all $\mathbf{e}_{\boldsymbol{\psi}_a}$ and $\mu > 0$, it is sufficient to show $\|\mathbf{e}_{\boldsymbol{\psi}_a}^{\mathrm{T}} \mathbf{e}_{\boldsymbol{\psi}_a}\| > \|\mathbf{e}_{\boldsymbol{\psi}_a}^{\mathrm{T}} \mathbf{K}_{\boldsymbol{\psi}_a}^{-1} (\boldsymbol{\lambda} - \hat{\boldsymbol{\lambda}})\|$ to prove that the time derivative of the Lyapunov function candidate is negative definite.

Assuming the bound on the generalized force error, (40), and applying the identity $\|\mathbf{e}_{\boldsymbol{\psi}_a}^{\mathrm{T}}\| \|\mathbf{e}_{\boldsymbol{\psi}_a}\| = \|\mathbf{e}_{\boldsymbol{\psi}_a}^{\mathrm{T}} \mathbf{e}_{\boldsymbol{\psi}_a}\|$ yields

$$\|\mathbf{e}_{\boldsymbol{\psi}_a}^{\mathrm{T}} \mathbf{e}_{\boldsymbol{\psi}_a}\| > \|\mathbf{e}_{\boldsymbol{\psi}_a}^{\mathrm{T}}\| \|\mathbf{K}_{\boldsymbol{\psi}_a}^{-1} (\boldsymbol{\lambda} - \hat{\boldsymbol{\lambda}})\|. \tag{45}$$

Applying the Schwarz inequality $\|\mathbf{e}_{\boldsymbol{\psi}_a}^{\mathrm{T}}\| \|\mathbf{K}_{\boldsymbol{\psi}_a}^{-1} (\boldsymbol{\lambda} - \hat{\boldsymbol{\lambda}})\| \geq \|\mathbf{e}_{\boldsymbol{\psi}_a}^{\mathrm{T}} \mathbf{K}_{\boldsymbol{\psi}_a}^{-1} (\boldsymbol{\lambda} - \hat{\boldsymbol{\lambda}})\|$ to (45), the condition on the generalized

force error assumed for stability can be expanded as

$$\|\mathbf{e}_{\boldsymbol{\psi}_a}^{\mathrm{T}}\,\mathbf{e}_{\boldsymbol{\psi}_a}\| > \|\mathbf{e}_{\boldsymbol{\psi}_a}^{\mathrm{T}}\,\mathbf{K}_{\boldsymbol{\psi}_a}^{-1}(\boldsymbol{\lambda}-\hat{\boldsymbol{\lambda}})\| \tag{46}$$

thus proving the stability of the controller given the bounds on the compensation error.

We note that the proof guarantees stability for estimation uncertainties $\boldsymbol{\lambda}-\hat{\boldsymbol{\lambda}}$ to be small with respect to the system error $\mathbf{e}_{\boldsymbol{\psi}_a}$. In order to maintain a stable pose in configurations close to the minimum of the generalized force (i.e., $\|\mathbf{K}_{\boldsymbol{\psi}_a}\,\mathbf{e}_{\boldsymbol{\psi}_a}\| \approx \|(\boldsymbol{\lambda}-\hat{\boldsymbol{\lambda}})\|$), the controller input must be filtered such that estimation error does not drive accidental motion. A dead-band filter is used to guarantee the controller acts only for deviation above a reasonable bound for the estimation error as will be described in the controller implementation below. The performance compromise of applying this filter is a reduction in controller responsiveness, where we define responsiveness as the minimal external force required to initiate compliant motion. The responsiveness will be evaluated in Section VI-C and methods for estimating $\hat{\boldsymbol{\lambda}}$ are discussed next.

C. Bounding the Generalized Force Error by ν-SVR Estimation

Error in canceling the generalized force uncertainties $\boldsymbol{\lambda}-\hat{\boldsymbol{\lambda}}$ bounds the responsiveness of the compliant motion controller (39). For small-load perturbations, the errors in the generalized force $\boldsymbol{\lambda}$ are well approximated by a function of the robot pose in configuration space $\boldsymbol{\psi}_a$, and the trajectory leading to this pose $\dot{\boldsymbol{\psi}}_a$, as friction depends on slip direction. The performance of the controller depends on canceling deviations from the idealized model. As specified in (38), this cancellation is carried out by a feed-forward term $\hat{\boldsymbol{\lambda}}$, which is obtained although offline training and online estimation of the model error via SVR.

The initial offline training produces data on the model uncertainties by exploring the workspace under unloaded conditions. In the absence of a perturbing wrench $\mathbf{w}_e$, measurement of the generalized force should be zero as described in (15) and (31). Therefore, any nonzero measurements during this data collection exploration constitute deviation from the model $\boldsymbol{\lambda}$.

SV machines provide a method for nonlinear regression through mapping of input vectors into a higher dimensional feature space [35], [36]. A subset of the training data from the *SVs* defines the parameters for regression. The choice of SVR stems from robustness, favorable generalization properties with noisy data, and compact structure allowing real-time function estimation during motion control.

To estimate the error in the generalized force based on an initial unloaded exploration of the workspace, the "ν" SV Regression (ν-SVR) [37] is used for each dimension of the generalized force. The ν-SVR algorithm provides a means for controlling the sparsity of SVs, therefore guaranteeing robustness to overfitting while simultaneously reducing the number of *a priori* control parameters.

The training set for the ν-SVR contains input pairs $\{\mathbf{x}_{[l]}, y_{[l]}\}_{l=1}^{N}$ based on the pose and measured generalized force gathered during the offline exploration in the absence of external perturbing forces. For the ith component of the generalized force, the input is given as

$$\mathbf{x}_{[l]} = \left[\frac{\boldsymbol{\psi}_{a,1}}{\max_N(\boldsymbol{\psi}_{a,1})},\ldots,\frac{\boldsymbol{\psi}_{a,2n}}{\max_N(\boldsymbol{\psi}_{a,2n})},\right.$$
$$\left.\frac{\dot{\boldsymbol{\psi}}_{a,1}}{\max_N(\dot{\boldsymbol{\psi}}_{a,1})},\ldots,\frac{\dot{\boldsymbol{\psi}}_{a,2n}}{\max_N(\dot{\boldsymbol{\psi}}_{a,2n})}\right]^{\mathrm{T}} \in \mathbb{R}^{4n}$$
$$y_{[l]} = \mathbf{f}_{a,i}|_{\mathbf{w}_e=\mathbf{0}} \tag{47}$$

where N is the number of training samples, $\max_N(\boldsymbol{\psi}_{a,i})$ is the maximum recorded magnitude of the ith row of $\boldsymbol{\psi}_a$ over the set $l \in [1, N]$, and $\dot{\boldsymbol{\psi}}_a$ is the configuration space velocity. This expression normalizes each element of the input vector $\mathbf{x}_{[l]}$ to the range of $[-1, 1]$ for all data in the training set.

Given these training input vector pairs, ν-SVR provides a method to estimate the feed-forward error correction function with each direction of the generalized force

$$\hat{\boldsymbol{\lambda}}_i(\mathbf{x}) = \langle \mathbf{a}, \boldsymbol{\varphi}(\mathbf{x})\rangle + b \tag{48}$$

where $\langle\cdot,\cdot\rangle$ is the inner product space, $\mathbf{a}$ and b are parameters to be determined by the convex optimization, and $\boldsymbol{\varphi}(\cdot) : \mathbb{R}^{4n} \rightarrow \mathbb{R}^{n_{\mathbf{x}h}}$ is a mapping of the input feature vector $\mathbf{x}_{[l]}$ to a higher dimensional feature space.

As specified in (48), the SVR algorithm allows mapping of the input space to a higher dimensional vector space. Uncertainties in predicting the generalized force, including friction and nonlinear bending, are well modeled by exponential functions [38], [39]. Given this intuition, a Gaussian radial basis function (RBF) kernel

$$k(\mathbf{x}_{[l]}, \mathbf{x}_{[m]}) = e^{-\gamma\|(\mathbf{x}_{[l]}-\mathbf{x}_{[m]})\|^2} \tag{49}$$

is chosen for higher dimensional mapping. The parameter, γ, of the RBF is tuned empirically while optimizing the parameters of the ν-SVR model.

The resulting ν-SVR model for function estimation with a new input vector, $\mathbf{x}^\star$, is given by

$$\hat{\boldsymbol{\lambda}}_i(\mathbf{x}) = \sum_{SV}(\boldsymbol{\alpha}_i^* - \boldsymbol{\alpha}_i)k(\mathbf{x}_{[i]}, \mathbf{x}^\star) + b. \tag{50}$$

It should be noted that only those training points $\{\mathbf{x}_{[l]}, y_{[l]}\}$, denoted SV in (50), for which $|y_{[l]} - \hat{\boldsymbol{\lambda}}_i(\mathbf{x}_{[l]})| \geq \epsilon$, form the SVs. During the computation of new estimates, only these SVs contribute to the final function estimation (50), thus enforcing sparsity in the regression.

VI. Experimental Evaluation

The evaluation of the compliant motion controller is next presented and discussed. First, the implementation of the controller is introduced. The methods for determining the feed-forward estimate with the ν-SVR algorithm are presented in addition to data displaying the efficacy in error reduction with this model. Responsiveness analysis subsequently provides an example of the effect of the dead-band filter on the controller's ability to respond to external wrenches. Finally, multiple experiments quantify the generalized force and external forces applied during blind insertion through tortuous passages unknown to the controller.

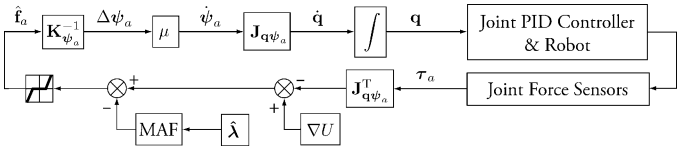

Fig. 4. Compliant motion controller. The compensation term $\hat{\boldsymbol{\lambda}}$ enters an MAF prior to entering the feedback loop. The feedback signal is filtered through a dead-band to minimize chattering.

A. Compliant Motion Controller Implementation

The real-time control for the compliant motion algorithm was implemented in a multirate controller under the MATLAB xPC computing environment. The main control loop updating the control values at the joint level ran at 1 kHz. Joint forces were measured at 5 kHz and smoothed with a moving average filter (MAF) and downsampled to the 1-kHz control loop. The SVR was run at 100 Hz as this rate reduced the overall computational burden of the controller while providing feed-forward estimates adequate to reduce the model error. An MAF smoothed outliers in the estimate provided by the SVR functions (50).

In order to reduce aberrant motions of the controller due to modeling and estimation errors, a dead-band filter was applied to the estimated generalized force to reduce joint motion due to uncompensated errors. The threshold of the dead-band filter for each direction of the generalized force was set appropriately for the expected errors after the application of the SVR.

Note that the controller relies on the invertibility of the configuration space stiffness. The block-diagonal matrix is constructed of the submatrices, $\mathbf{K}_{\boldsymbol{\psi},(k)}$, as in (33). Singular configurations of $\mathbf{K}_{\boldsymbol{\psi},(k)}$, and therefore $\mathbf{K}_{\boldsymbol{\psi}_a}$, correspond with a straight segment, $\theta_{(k)} = \frac{\pi}{2}$. For control purposes, the effect of singular poses can be mitigated using a singularity robust inverse of the configuration space stiffness [40].

The resulting compliant motion controller, based on (39) and taking into account the estimates from the ν-SVR, is given in Fig. 4. Without application of the feed-forward SVR error correction, the controller was immediately unstable without dead-band filter values exceeding forces damaging to the robot structure, as the errors without correction exceeded the threshold of the dead-band independent of the robot pose.

B. SVR Implementation for Error Estimation

The software LibSVM [41] was used to determine the optimal parameters of ν-SVR model for function estimation (50). To train the SVR, data for a training sample set, including the robot pose, trajectory, actuation forces, and measured generalized forces, were collected at 125 Hz during an unloaded motion in the configuration space of a two-segment continuum robot. The trajectories in each configuration space variable $\theta_{(1)}$, $\delta_{(1)}$, $\theta_{(2)}$, and $\delta_{(2)}$, are uncorrelated to provide a robust dataset for estimation. Thus, the individual sections are moving in independent trajectories through points encompassing the full workspace of each section, entering these points via non-correlated paths without returning to an initial start configuration. Data collection can be seen in the multimedia extension to this paper. Data from the workspace exploration are segmented evenly into training and validation sets.

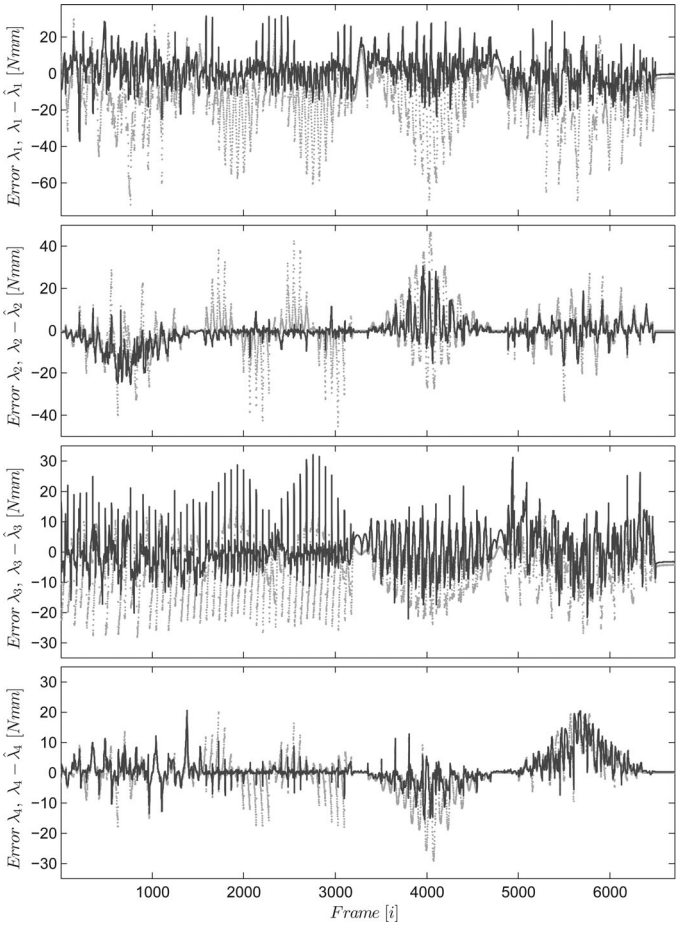

Fig. 5. ν-SVR error compensation for all components of the error compensation of the generalized force. Light gray points denote the measured error in the generalized force $\boldsymbol{\lambda}$. Dark gray lines denote the ν-SVR compensated error $\boldsymbol{\lambda} - \hat{\boldsymbol{\lambda}}$.

TABLE I
MEAN ERROR AND VARIANCE FOR THE GENERALIZED FORCE DIRECTIONS WITH AND WITHOUT ν-SVR COMPENSATION

Direction	Mean Error [Nmm]		Variance [(Nmm)^2]		Std. Dev. [Nmm]	
	Uncomp.	Comp.	Uncomp.	Comp.	Uncomp.	Comp.
θ_1	20.15	8.08	252.53	64.69	15.89	8.04
δ_1	9.93	5.94	98.61	34.25	9.93	5.85
θ_2	10.26	6.21	77.06	38.58	8.78	6.21
δ_2	5.90	4.30	34.76	17.71	5.90	4.21

The ν-SVR displays good generalization to untrained data as reflected in the significant reduction in error in the generalized force. The measured generalized force error $\boldsymbol{\lambda}$ and error after correction $\boldsymbol{\lambda} - \hat{\boldsymbol{\lambda}}$ are presented for the validation subset of a sample dataset in Fig. 5. Frames displayed in Fig. 5 are given for every tenth collected sample. Table I provides the mean error and variance of the validation dataset with and without compensation. The compensation provides a minimum of 1.4 times reduction in the RMS error for $\boldsymbol{\lambda}_4$ and a maximum of 2.5 times reduction for $\boldsymbol{\lambda}_1$.

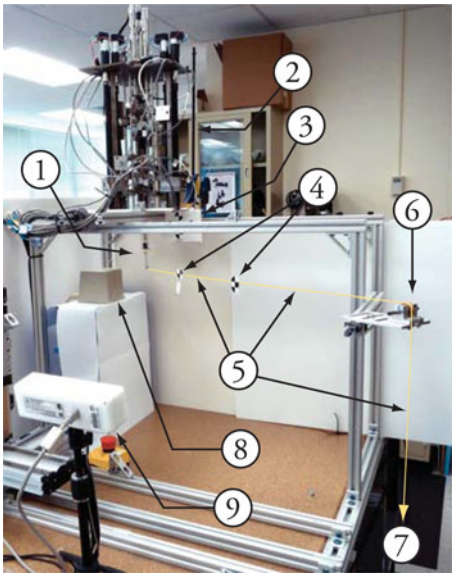

Fig. 6. Experimental setup for responsiveness analysis. The system consists of the single segment continuum robot with the attached magnetic sensors ①, actuation unit ②, optical tracker markers for the system base orientation ③, optical tracker markers for the load vector ④, Kevlar thread ⑤, pulley ⑥, Ascension trakStar magnetic tracker base ⑧, Claron Micron optical tracker ⑨. Calibrated weights are attached to the Kevlar thread at ⑦.

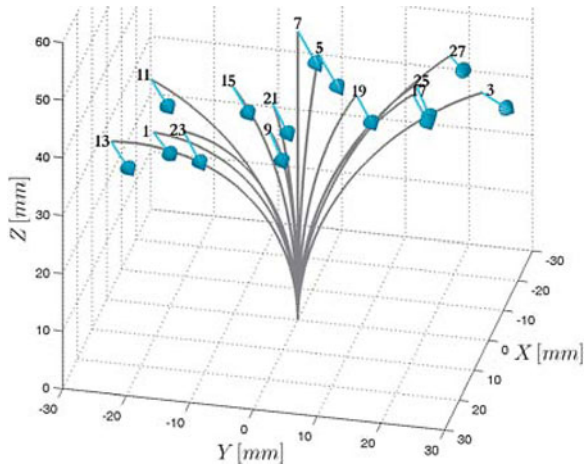

Fig. 7. Distribution of the numbered poses (odd-numbered shown) sampled during responsiveness evaluation of the compliant motion controller. Each labeled curve designates the shape of the primary backbone and the direction vector of the applied force.

C. Responsiveness Analysis

The previous sections introduced a controller with a feedforward term for model uncertainty compensation. The sum of the uncertainty estimate and the expected generalized force is filtered through a dead band (see Fig. 4) to prevent erroneous motion. Thus, generalized forces below the dead-band threshold will be neglected. The threshold for this filter, therefore, forms a tradeoff between the responsiveness to external perturbations and insensitivity to errors in the model and compensation.

To demonstrate the effects of the controller and thresholding, the responsiveness of the controller to external wrenches was quantified on a single-segment continuum robot. The experimental setup shown in Fig. 6 used a single-stage multibackbone continuum robot with actuation force sensing capability and originally described in [25]. The proximal ends of the secondary backbones of the continuum robot are coupled through inline load cells (Omega Engineering, Inc., Model LC703-10) to the lead-screw-driven actuation stages. A wrench was applied at the end disk of the segment ① by a Kevlar thread ⑤, and attached through a pulley system ⑥ to calibrated weights ⑦. The load direction at each pose was measured relative to the robot's base using a MicronTracker H-40 optical tracker (Claron Technologies), with a specified accuracy of 0.20-mm RMS. Optical markers mounted to the Kevlar thread ④, and to the base of the continuum robot ③, specify the direction of the applied force. The weight of the thread and markers is less than 1 g and is negligible with respect to the loads required to initiate the compliant motion.

The Micron system provides a specification for the linear accuracy of the device, while the experiment requires an orientation measurement. The linear accuracy can be used to estimate the orientation accuracy of the Micron tracking system by noting that the orientation of a vector is calculated based on the position of two marker points. The smallest linear distance between marker points of 48.5 mm used for the orientation estimation occurs at the base marker system ③. (Although the direction marker perpendicular to the thread is significantly shorter, this direction is not used to compute the direction of the Kevlar thread.) An RMS error of 0.2 mm at a moment of 24.25 mm results in an error smaller than 0.5°.

For the responsiveness measurement at each pose, the segment was guided into position by manually applying an external wrench and allowing the continuum structure to comply to the sampled configuration. The pose estimate was measured via the nominal kinematics and was verified by an embedded magnetic tracker system (Ascension Technology 3-D Guidance trakStar) ⑧, with an RMS orientation accuracy of 0.5°. The load direction was measured via the optical trackers after a 10-g weight was applied to the Kevlar thread to straighten the thread length between the optical markers. Calibration weights were added to the load in 1-g increments until the threshold for motion was exceeded. This threshold for motion is exactly the external force required to achieve a generalized force greater than the dead-band cutoff and therefore induce motion of the system. The controller's dead-band was specified throughout the responsiveness experiment as

$$\|\mathbf{f}_1\| \leq 20 \text{ N·mm}, \ \|\mathbf{f}_2\| \leq 10 \text{ N·mm}. \tag{51}$$

These thresholds were determined based on the error compensation in the generalized force using SVR as described in Section VI-B.

Responsiveness measurements were recorded for 28 poses shown for the odd-numbered samples in Fig. 7. Poses were selected throughout the workspace to ensure a distribution with load directions varying relative to the pose angle δ. The mean perturbation force required to induce motion under the experimental conditions was 0.99 N with a standard deviation of 0.28 N. The maximal force required to induce motion was 1.5 N.

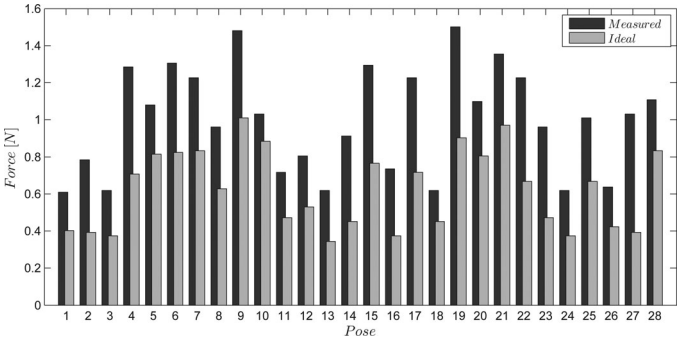

Fig. 8. The required minimal forces for motion in each measured pose. The ideal force corresponds to the force required to exceed the dead-band filter threshold on the compensated generalized force $\hat{\mathbf{f}}$ assuming $\boldsymbol{\lambda} = 0$.

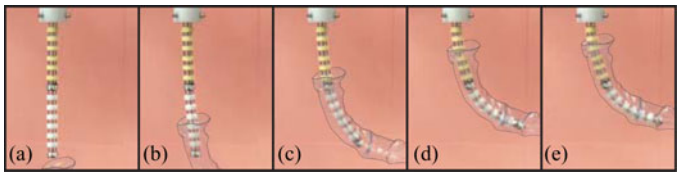

Fig. 9. Compliant insertion demonstration illustrating individual frames from multimedia extension. An acrylic tube with a 3-D shape is guided into contact with the continuum robot in a method analogous to instrument contact during insertion. The multiple contacts between the robot and the tube are present during the insertion. The edges of the acrylic tube are highlighted by a dotted line in each frame.

Under ideal conditions in which the generalized force is undisturbed by uncertainty (15), the applied force required to induce motion can be calculated as the minimum force required to exceed the motion threshold defined by (51). The minimum force required to exceed the threshold in the direction of the applied force based on the idealized model is provided in addition to the measured force in Fig. 8.

The responsiveness measurements provide an opportunity to evaluate the contribution of the model uncertainties and the compensation by ν-SVR. The average difference between the measured and ideal force was 0.37 N with a standard deviation of 0.14 N, corresponding to a model error relative to the actual measurement of 37.5 percent. Thus, the data show that model uncertainty contributes significantly to the responsiveness of the controller. Furthermore, without this feed-forward term, the controller would be overwhelmed by the uncertainties of the system or require a dead-band filter threshold value that would prevent active compliance at forces sufficiently low to prevent damage to the robot or environment. Improvement to the mechanical construction of the robot to reduce friction may remove errors and increase the responsiveness. We note that this experiment is limited to measuring the responsiveness of the compliant motion controller to forces acting at the tip of the segment. If a force acts at a different location of the segment, it is tantamount to the same force acting at the tip of the segment with an added couple. Therefore, forces acting at unknown locations along the length of the segment produce a reaction to this input as demonstrated in the following sections.

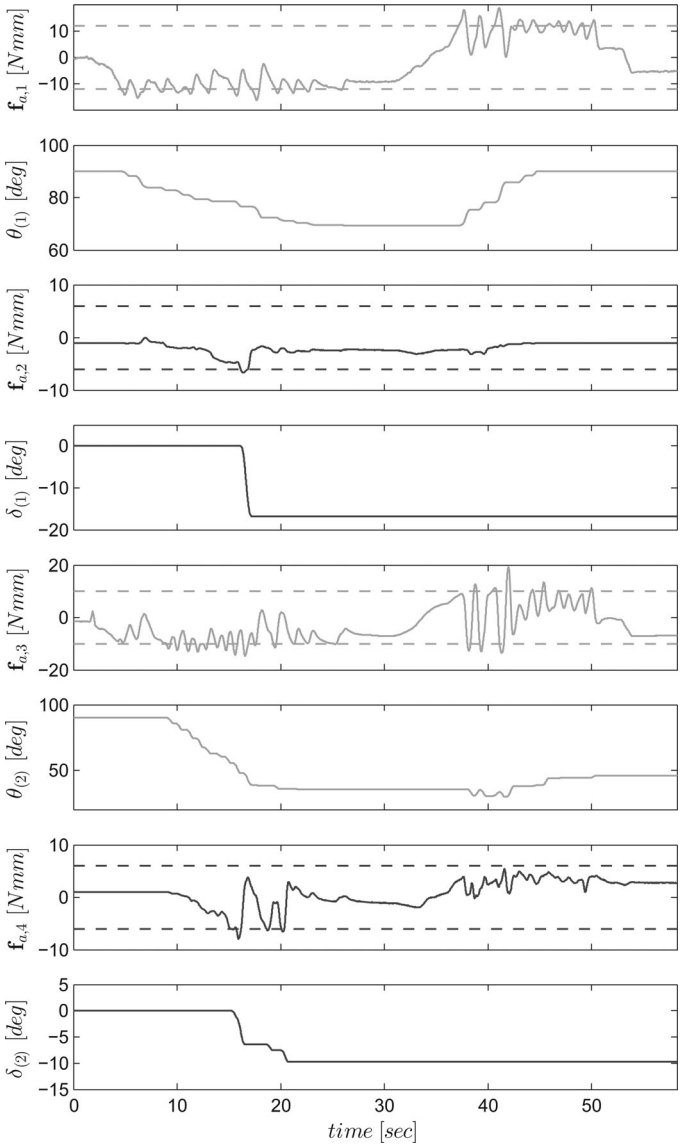

Fig. 10. Reaction data for the compliant insertion. Each component of the generalized force and the configuration space for the two-segment stage is displayed separately. The dashed lines demarcate the upper and lower threshold on the generalized force for motion.

D. Compliant Insertion

1) Ø9 mm Two-Segment Robot in Rigid 3D-Shaped Tube: To evaluate the controller applicability, a two-segment continuum robot was inserted into an acrylic tube with a 3-D shape comprised of multiple out-of-plane bends. The robot was driven by the actuation unit described in Section VI-C. The acrylic tube was mounted to an insertion stage that autonomously, and independent of the continuum robot controller, brought the tube into contact with the robot in a manner analogous to blind insertion into a cavity and subsequent retraction. The insertion stage impedance is high with respect to the compliance controller and, therefore, does not significantly affect the overall compliance control of the system. The controller had no prior knowledge of the geometry of the tube or the path plan of the insertion stage. The controller successfully complied with the confined

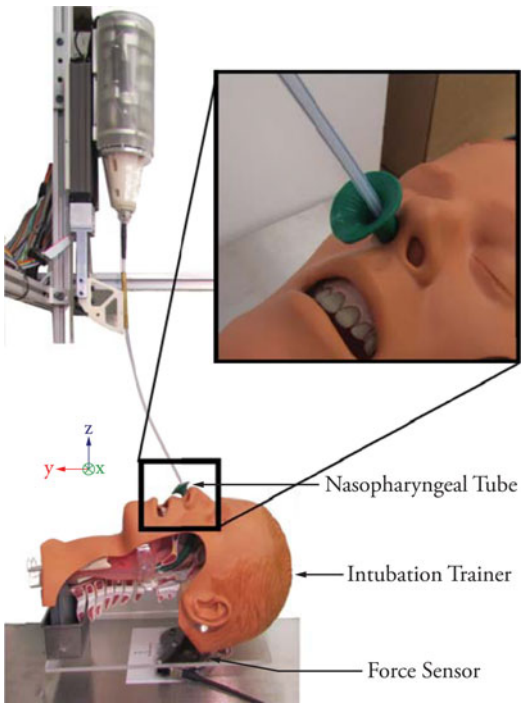

Fig. 11. The experimental setup from [42] consists of a ⌀5 mm continuum robot with flexible actuation lines, a 34Fr nasopharyngeal tube, a Nasco AMBU intubation trainer, and an ATI Gamma force/torque sensor.

complex shape despite a moving contact location unknown to the controller, as depicted in Fig. 9 and in the multimedia extension.

The estimates of the generalized force $\mathbf{f}_a \triangleq [\mathbf{f}_{a,1}, \mathbf{f}_{a,2}, \mathbf{f}_{a,3}, \mathbf{f}_{a,4}]^T$ during insertion and retraction are presented in Fig. 10. The data display the effect of the threshold on the motion of the system when subject to external perturbations. Magnitudes of $\mathbf{f}_a$ below the threshold for compliant motion, denoted by the dashed lines in Fig. 10, are filtered and do not cause motion of the robot. As $\mathbf{f}_a$ exceeds the threshold, the controller rapidly moves to reduce the force to a level below the threshold.

2) Ø5 mm Two-Segment Robot in Intubation Trainer: In order to evaluate the feasibility of deployment in the geometric equivalent of human anatomy, a Ø5 mm two-segment continuum robot was inserted through the nasopharyngeal cavities of the Nasco AMBU Intubation Trainer to access the laryngopharynx, as shown in Fig. 11. This robot was originally described in [43], and a detailed clinical motivation and experiments for transnasal access were presented in [42]. The robot was brought into contact with the orifice of a nasopharyngeal airway inserted through nasopharynx of the mannikin and then advanced through to the larynx under the compliant control algorithm. Forces exerted on the mannikin were recorded using an industrial force sensor (ATI Industrial Automation, Model Gamma SI-130-10). In order to reduce friction, the stem was lubricated with water-soluble lubricant typically used in otolaryngology procedures (MediChoice 1365063021).

Nine insertions were performed and data from individual experiments were correlated by the initial increase in the force exerted on the manikin. These correlated data are presented in Fig. 12 illustrating the average force and variation across all

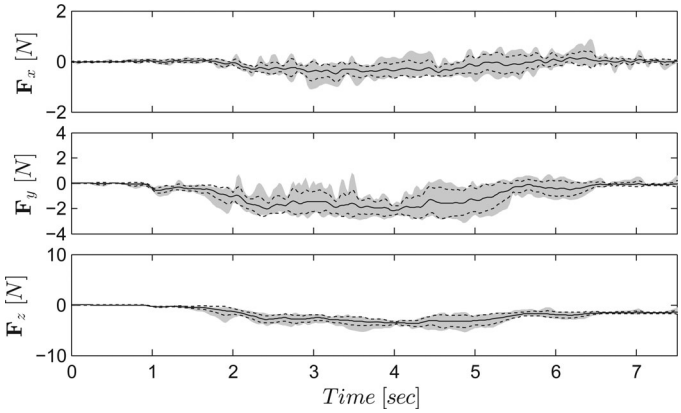

Fig. 12. Forces exerted on the manikin during insertion trials with compliant motion control. The solid line represents the average force across insertion trials. Dashed lines provide the standard deviation, and the shaded area represents the maximum and minimum forces across insertion trials.

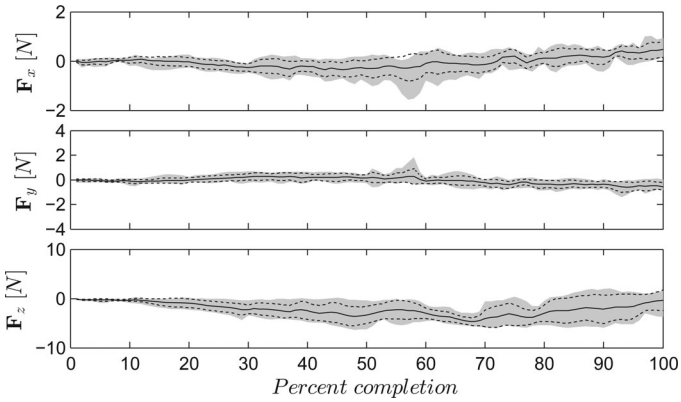

Fig. 13. Forces exerted on the manikin during passive insertion trials. Abscissa represents percent completion to full insertion The solid line represents the average force across insertion trials. Dashed lines provide the standard deviation, and the shaded area represents the maximum and minimum forces across insertion trials.

insertions at each time point during the insertions. The average maximum insertion forces over the nine insertion trials in the *x*-, *y*-, and *z*-directions were 0.86 N (range 0.65–1.22 N), 2.70 N (range 2.41–3.14 N), and 4.54 N (range 3.74–5.40 N), respectively. In addition, the average insertion speed was 34 mm/s for an inserted portion of 200 mm with an average insertion time of 5.87 s.

To evaluate the effect of the compliant motion controller, we also repeated the insertions using the same setup but without compliant motion control (passive compliance). Inserting the robot while connected to the actuation unit without active compliance was not possible because the forces would exceed the breaking forces of the backbones. Thus, the robot stem was disconnected from its actuation unit during these experiments. Fig. 13 shows the results of nine experiments. The average maximum insertion forces over the nine insertion trials in the *x*-, *y*-, and *z*-directions were 0.83 N (range 0.54–1.57 N), 1.05 N (range 0.68–1.82 N), and 5.67 N (range 4.77–6.35 N), respectively. The insertion experiments could not be actualized with uniform times due to the robot tip jamming against the

nasopharyngeal tube. Hence, the figure displays percentage to full insertion instead of time.

The forces with active compliance are comparable with the forces when using a passively flexible stem. Thus, the controller provides a method for compliant interaction while maintaining active control of the robot DoF. These forces are distributed along the length of the robot during insertion. While there are no works directly reporting forces during trans-nasal access of the laryngopharynx, we note with similar force levels, we have been successful in gaining access into cadavers without damaging the anatomy [44].

VII. Conclusion

Continuum robots enable deep reach into confined and unstructured environments. The use of these robots for insertion and exploration creates complex contacts along the robot backbone. The challenge addressed by this paper is a controller design for compliant motion of continuum robots without knowledge of contact locations. The method employs a mapping of the unknown interaction forces into a generalized force in the configuration space of a continuum segment. Errors in the estimated and actual generalized force were used to drive the system to minimize the external perturbing forces. The work demonstrated the use of SVR to estimate unmodeled nonlinear effects of friction and bending in continuum robots. The solution further provided a simplified formulation for unloaded stiffness of compliant robot segments. This simplified stiffness model was then used to drive a compliant motion controller.

We believe that the framework developed in this study enables a new class of robots capable of safe insertion into unstructured environments while preventing self or environmental damage. In our recent preliminary work [44], the success of the presented compliant control approach was demonstrated in enabling trans-nasal access into the upper airways of a human cadaver. Full evaluation of the safety of the compliant controller in surgical scenarios requires more thorough future validation in cadavers and live animal models.

References

[1] S. Hirose, *Biologically Inspired Robots: Snake-like Locomotors and Manipulators*. New York, NY, USA: Oxford Univ. Press, 1993.

[2] G. Robinson and J. B. C. Davies, "Continuum robots—A state of the art," in *Proc. IEEE Int. Conf. Robot. Autom.*, Detroit, MI, USA, 1999, pp. 2849–2854.

[3] R. J. Webster and B. A. Jones, "Design and kinematic modeling of constant curvature continuum robots: A review," *Int. J. Robot. Res.*, vol. 29, no. 13, pp. 1661–1683, Jun. 2010.

[4] H. Tsukagoshi, A. Kitagawa, and M. Segawa, "Active hose: An artificial elephant's nose with maneuverability for rescue operation," in *Proc. IEEE Int. Conf. Robot. Autom.*, Seoul, Korea, 2001, pp. 2454–2459.

[5] T. Aoki and S. Hirose, "Development of slime robot using bridle bellows," *J. Robot. Mechatron.*, vol. 16, no. 3, pp. 286–292, 2004.

[6] G. Immega and K. Antonelli, "The KSI tentacle manipulator," in *Proc. IEEE Int. Conf. Robot. Autom.*, Nagoya, Japan, 1995, pp. 3149–3154.

[7] N. Simaan, "Snake-like units using flexible backbones and actuation redundancy for enhanced minaturization," in *Proc. IEEE Int. Conf. Robot. Autom.*, Barcelona, Spain, 2005, pp. 3023–3028.

[8] N. Simaan, K. Xu, A. Kapoor, W. Wei, P. Kazanzides, P. Flint, and R. Taylor, "Design and integration of a telerobotic system for minimally invasive surgery of the throat.," *Int. J. Robot. Res.*, vol. 28, no. 9, pp. 1134–1153, Sep. 2009.

[9] D. B. Camarillo, C. R. Carlson, and J. K. Salisbury, "Configuration tracking for continuum manipulators with coupled tendon drive," *IEEE Trans. Robot.*, vol. 25, no. 4, pp. 798–808, Aug. 2009.

[10] H.-S. Yoon and B.-J. Yi, "A 4-DOF flexible continuum robot using a spring backbone," in *Proc. IEEE Int. Conf. Mechatron. Autom.*, Changchun, China, 2009, pp. 1249–1254.

[11] R. S. Dahiya, G. Metta, M. Valle, and G. Sandini, "Tactile sensing—From humans to humanoids," *IEEE Trans. Robot.*, vol. 26, no. 1, pp. 1–20, Feb. 2010.

[12] K. Salisbury, W. Townsend, B. Ebrman, and D. DiPietro, "Preliminary design of a whole-arm manipulation system (WAMS)," in *Proc. IEEE Int. Conf. Robot. Autom.*, Philadelphia, PA, USA, 1988, pp. 254–260.

[13] H. Mochiyama, E. Shimemura, and H. Kobayashi, "Shape control of manipulators with hyper degrees of freedom," *Int. J. Robot. Res.*, vol. 18, no. 6, pp. 584–600, Jun. 1999.

[14] J. Park and O. Khatib, "Robot multiple contact control," *Robotica*, vol. 26, no. 5, pp. 667–677, Sep. 2008.

[15] I. A. Gravagne and I. D. Walker, "Manipulability, force, and compliance analysis for planar continuum manipulators," *IEEE Trans. Robot. Autom.*, vol. 18, no. 3, pp. 263–73, Jun. 2002.

[16] K. Ikuta, K. Sasaki, K. Yamamoto, and T. Shimada, "Remote microsurgery system for deep and narrow space development of new surgical procedure and micro-robotic tool sophisticated medical treatment and cases," in *Proc. 5th Int. Conf. Med. Image Comput. Comput.-Assist. Intervention*, Tokyo, Japan, 2002, pp. 163–172.

[17] S. Aramaki, S. Kaneko, K. Arai, Y. Takahashi, H. Adachi, and K. Yanagisawa, "Tube type micro manipulator using shape memory alloy (SMA)," in *Proc. IEEE 6th Int. Symp. Micro Mach. Human Sci.*, Nagoya, Japan, 1995, pp. 115–120.

[18] S. Maeda, K. Abe, K. Yamamoto, O. Tohyama, and H. Ito, "Active endoscope with SMA (shape memory alloy) coil springs," in *Proc. IEEE 9th Annu. Int. Workshop Micro Electro Mech. Syst.*, San Diego, CA, USA, 1996, pp. 290–295.

[19] P. Dario, C. Paggetti, N. Troisfontaine, E. Papa, T. Ciucci, M. C. Carrozza, and M. Marcacci, "A miniature steerable end-effector for application in an integrated system for computer-assisted arthroscopy," in *Proc. IEEE Int. Conf. Robot. Automat.*, Albuquerque, NM, USA, 1997, pp. 1573–1579.

[20] J. Jayender, R. V. Patel, and S. Nikumb, "Robot-assisted active catheter insertion: Algorithms and experiments," *Int. J. Robot. Res.*, vol. 28, no. 9, pp. 1101–1117, May 2009.

[21] K. Ikuta, H. Ichikawa, K. Suzuki, and D. Yajima, "Multi-degree of freedom hydraulic pressure driven safety active catheter," in *Proc. IEEE Int. Conf. Robot. Automat.*, Orlando, FL, USA, 2006, pp. 4161–4166.

[22] G. Chen, M. T. Pham, and T. Redarce, "Sensor-based guidance control of a continuum robot for a semi-autonomous colonoscopy," *Robot. Autonom. Syst.*, vol. 57, no. 6–7, pp. 712–722, Jun. 2009.

[23] M. Mahvash and P. E. Dupont, "Stiffness control of surgical continuum manipulators," *IEEE Trans. Robot.*, vol. 27, no. 2, pp. 334–345, Apr. 2011.

[24] N. Giri and I. Walker, "Continuum robots and underactuated grasping," *Mech. Sci.*, vol. 2, no. 1, pp. 51–58, 2011.

[25] K. Xu and N. Simaan, "An investigation of the intrinsic force sensing capabilities of continuum robots," *IEEE Trans. Robot.*, vol. 24, no. 3, pp. 576–587, Jun. 2008.

[26] K. Xu and N. Simaan, "Analytic formulation for kinematics, statics, and shape restoration of multibackbone continuum robots via elliptic integrals," *ASME J. Mech. Robot.*, vol. 2, no. 1, Nov. 2009.

[27] A. Bajo and N. Simaan, "Kinematics-based detection and localization of contacts along multisegment continuum robots," *IEEE Trans. Robot.*, vol. 28, no. 2, pp. 291–302, Apr. 2012.

[28] R. E. Goldman, A. Bajo, and N. Simaan, "Compliant motion control for continuum robots with intrinsic actuation sensing," in *Proc. IEEE Int. Conf. Robot. Autom.*, Shanghai, China, 2011, pp. 1126–1132.

[29] B. A. Jones and I. D. Walker, "Practical kinematics for real-time implementation of continuum robots," *IEEE Trans. Robot.*, vol. 22, no. 6, pp. 1087–1099, Dec. 2006.

[30] P. Dupont, J. Lock, B. Itkowitz, and E. Butler, "Design and control of concentric-tube robots," *IEEE Trans. Robot.*, vol. 26, no. 2, pp. 209–225, Apr. 2010.

[31] B. Siciliano and L. Villani, *Robot Force Control*. Boston, MA, USA: Kluwer, 1999.

[32] S.-F. Chen, "Conservative congruence transformation for joint and cartesian stiffness matrices of robotic hands and fingers," *Int. J. Robot. Res.*, vol. 19, no. 9, pp. 835–847, 2000.

[33] B.-J. Yi, G. B. Chung, H. Y. Na, and W. K. Kim, "Design and experiment of a 3-DOF parallel micromechanism utilizing flexure hinges," *IEEE Trans. Robot. Autom.*, vol. 19, no. 4, pp. 604–612, Aug. 2003.

[34] K. Xu and N. Simaan, "Actuation compensation for flexible surgical snake-like robots with redundant remote actuation," in *Proc. IEEE Int. Conf. Robot. Autom.*, Orlando, FL, USA, 2006, pp. 4148–4154.
[35] V. N. Vapnik, *Statistical Learning Theory*. New York, NY, USA: Wiley-Interscience, 1998.
[36] B. Schölkopf and A. J. Smola, *Learning with Kernels*. Cambridge, MA, USA: MIT Press, 2001.
[37] B. Schölkopf, A. Smola, R. Williamson, and P. Bartlett, "New support vector algorithms," *Neural Comput.*, vol. 12, no. 5, pp. 1207–45, May 2000.
[38] H. Olsson, K. Astrom, C. de Wit, M. Gafvert, and P. Lischinsky, "Friction models and friction compensation," *Eur. J. Control*, vol. 4, no. 3, pp. 176–195, 1998.
[39] R. Merzouki, J. C. Cadiou, and N. K. M'Sirdi, "Compensation of friction and backlash effects in an electrical actuator," *J. Syst. Control Eng.*, vol. 218, no. 2, pp. 75–84, Mar. 2004.
[40] Y. Nakamura, *Advanced Robotics: Redundancy and Optimization*. Reading, MA, USA: Addison-Wesley, 1991.
[41] C.-C. Chang and C.-J. Lin. (2001). *LIBSVM: A library for support vector machines* [Online]. Available: http://www.csie.ntu.edu.tw/ cjlin/libsvm
[42] A. Bajo, L. M. Dharamsi, J. L. Netterville, C. G. Garrett, and N. Simaan, "Robotic-assisted micro-surgery of the throat: The trans-nasal approach," in *Proc. IEEE Int. Conf. Robot. Autom.*, Karlsruhe, Germany, 2013, pp. 232–238.
[43] R. E. Goldman, A. Bajo, L. S. MacLachlan, R. Pickens, S. D. Herrell, and N. Simaan, "Design and performance evaluation of a minimally invasive telerobotic platform for transurethral surveillance and intervention," *IEEE Trans. Biomed. Eng.*, vol. 60, no. 4, pp. 918–925, Apr. 2013.
[44] A. Bajo, L. Dharamsi, J. Netterville, C. Garrett, and N. Simaan, "Trans-nasal robotic micro-surgery of the throat: A cadaveric feasibility study," presented at the Hamlyn Symp. Med. Robot., London, U.K., 2013, pp. 27–28

Roger E. Goldman (S'07–M'13) received the B.Sc. degree in mechanical engineering from Stanford University, Stanford, CA, USA, in 2002 and the Ph.D. degree in biomedical engineering and the M.D. degree from Columbia University, New York, NY, USA, in 2012 and 2013, respectively.

He is currently a transitional year Medical Intern with the Department of Medicine, Crozer Chester Medical Center, Upland, PA, USA, and will begin a residency in diagnostic radiology with Stanford University in 2014.

Andrea Bajo (S'10–M'13) received the Laurea degree in control engineering from the University of Rome "La Sapienza," Rome, Italy, in 2007, the M.Sc. degree in mechanical engineering from Columbia University, New York, NY, USA, in 2009, and the Ph.D. degree in mechanical engineering from Vanderbilt University, Nashville, TN, USA, in 2013.

He is currently a System Research Engineer at MAKO Surgical Corp., Fort Lauderdale, FL, USA.

Nabil Simaan (SM'04) received the Ph.D. degree in mechanical engineering from the Technion–Israel Institute of Technology, Haifa, Israel, in 2002.

In 2003, he was a Postdoctoral Research Scientist with Johns Hopkins University National Science Foundation Engineering Research Center for Computer-Integrated Surgical Systems and Technology, Baltimore, MD, USA, where he investigated minimally invasive robotic assistance in confined spaces. In 2005, he joined Columbia University, New York, NY, USA, as an Assistant Professor. He was promoted to Associate Professor in 2010 and, subsequently, joined Vanderbilt University, Nashville, TN, USA, in the Fall of 2010.

Dr. Simaan received the NSF Career Award to design new algorithms and robots for safe interaction with the anatomy in 2009.